Large X-ray time lags from compact black hole coronae

Phil Uttley[1][*] and Julien Malzac[2,3]

[1] *Anton Pannekoek Institute, University of Amsterdam, Science Park 904, 1098 XH Amsterdam, The Netherlands*
[2] *Université de Toulouse, UPS-OMP, IRAP, Toulouse, France*
[3] *CNRS, IRAP, 9 Av. colonel Roche, BP44346, F-31028 Toulouse cedex 4, France*

Submitted...

ABSTRACT
Stuff

Key words: X-rays: binaries - X-rays: individual (GRO J1655-40) - accretion, accretion discs

1 INTRODUCTION

The spectral energy distributions of accreting black holes across the mass scale, from X-ray binaries (BH XRBs) to Active Galactic Nuclei (AGN), show a ubiquitous power-law continuum component, as well as evidence for a blackbody emitting accretion disk and X-ray reflection features (iron line and Compton hump) produced by reprocessing of the power-law flux that is incident on the disk. It was understood early on that the X-ray power-law is produced by inverse Compton scattering of lower energy 'seed' photons by hot ($\sim 10^8 - 10^9$ K) plasma (Shapiro et al. 1976). Constraints from the power-law index and the presence of a cut-off or roll-over at energies of tens of keV or greater, suggest predominantly thermal Comptonisation, with moderate optical depths $\tau \sim 1$ (e.g. Zdziarski et al. 1998; Makishima et al. 2008; Zoghbi et al. 2017), and the seed photons likely originate in the disk (Done et al. 2007). The X-ray reflection features show that the disk reprocesses at least tens of per cent of the power-law luminosity, implying that the power-law emitting region has some vertical extent compared to the thin disk. Thus we can refer to this hot, Compton-scattering region as a 'corona' without making any further assumptions about its geometry.

The X-ray emission of all accreting black holes is variable over a range of time-scales and significant new information is provided by X-ray spectral-timing, such as the measurement of time lags between variations of photons at different energies (see Uttley et al. 2014 for a review). Time delays of hard photons relative to soft photons (so-called 'hard lags'), which increase with variability time-scale (to the equivalent of thousands of gravitational radii, R_g in light-crossing time), have been known for several decades, in both BH XRBs (e.g. Miyamoto et al. 1988; Nowak et al. 1999) and AGN (e.g. Papadakis et al. 2001; Arévalo et al. 2006). The origin of the hard lags remains unclear but they have been variously linked to energy-dependent light-travel delays imposed by Compton up-scattering in a highly extended spherical corona (Kazanas et al. 1997; Kroon & Becker 2016) or jet (Reig et al. 2003;

Giannios et al. 2004), the spectral evolution of coronal magnetic flares (Poutanen & Fabian 1999; Böttcher 2001), or the inward propagation of waves (Misra 2000) or mass accretion fluctuations (Kotov et al. 2001; Arévalo & Uttley 2006; Rapisarda et al. 2016) through a hot, Comptonising accretion flow.

In the past decade, X-ray lags have been studied in increasing detail in AGN and BHXRBs, notably on shorter time-scales with better data and more sensitive techniques, which reveal a switch in sign to small (equivalent to $< 10\ R_g/c$ in light-crossing time) soft lags in both AGN (e.g. Fabian et al. 2009; De Marco et al. 2013), and BHXRBs (Uttley et al. 2011; De Marco et al. 2015), as well as clear (and model-independent) reflection signatures in the lags, when the detailed dependence of lag versus energy is plotted for AGN (e.g. Zoghbi et al. 2012; Kara et al. 2015). The small lags and evidence for associated reflection delays suggest that the switch to soft lags is linked to X-ray reverberation: the light-travel delay of photons which reprocess off the disk on their way to the observer. The small lags then also imply small coronae, consistent with the relativistically broadened reflection reflection features observed in the X-ray spectra, which require relatively small (tens of R_g or smaller) inner disk radii with corresponding steep radial illumination profiles (Nowak et al. 2011; Miller et al. 2015). Small (sub-10 R_g) coronal sizes are also inferred from X-ray microlensing studies of quasars (e.g Chartas et al. 2009; MacLeod et al. 2015).

The compact coronae inferred from the short time-scale lags and relativistic reflection are fundamentally in tension with existing models for the longer time-scale hard lags. Based on the lack of reflection evidence for extended illumination of the accretion disk, we can already rule out the extended corona and jet models for the lags, which imply significant X-ray emission from scales thousands of R_g above the disk. However, even the 'propagating fluctuation' models, where the large lags are produced by relatively slow viscous propagation of mass accretion fluctuations through a power-law emitting region, require some significant radial extent of the emitting region (Arévalo & Uttley 2006). This is because the variations propagate inwards on a viscous time-scale which must be relatively fast, perhaps only ten times the dynamical time-scale, for the type of geometrically thick

hot flow required to explain the lags. For this reason, efforts to integrate the hard power-law lags and the reverberation lags have invoked more complex two-component emitting regions, with a radially extended corona combined with a more compact central corona to produce the reverberation signal (Wilkins et al. 2016).

In this paper, we resolve the tension between short reverberation lags and long power-law lags while requiring only a simple compact corona, by showing that large hard lags from the power-law emission are a natural consequence of accretion fluctuations which propagate through the disk *before* reaching the corona, even if the corona is < 10 R_g in scale. Since the seed photons are modulated by the fluctuations before the corona is heated by them, the corona cools and then heats after a large, viscous time-scale delay, to produce large lags even for small coronae and inner disk radii. This picture is strongly supported by *XMM-Newton* measurements of lags down to soft X-rays in BH XRB hard states, which clearly show that the disk blackbody emission varies before the power-law emission (Uttley et al. 2011; De Marco et al. 2015).

In Section 2 we use an impulse response function approach to show that hard power-law lags with a log-linear energy dependence (as seen in the data) are automatically produced when the seed photons from the disk are seen to vary before a fluctuation reaches the corona. In Section **??** we develop a numerical realisation of this model which we use in Section 4 to show that, for moderate coronal sizes and if reverberation is also included, the model can naturally reproduce the amplitudes and Fourier frequency-dependences of the observed disk-to-power-law leads and hard power-law lags. We discuss our model implications and its limitations in Section **??**, before setting out our conclusions in Section **??**. In the Appendix we use numerical Monte Carlo simulations of variable accretion to demonstrate the validity of our impulse response approach in the non-linear variability regime.

2 TIME RESPONSE OF CORONAL EMISSION

We consider Comptonising coronae in thermal equilibrium, where the instantaneous photon index Γ is set by the ratio of the time-dependent input seed luminosity (L_s) to heating luminosity (L_h) as follows:

$$\Gamma(t) = \Gamma_0 \left(\frac{L_\mathrm{s}(t)}{L_\mathrm{h}(t)} \right)^{\beta} \quad , \qquad (1)$$

where Γ_0 is the photon index for equal seed and heating luminosities and β is an index which may be derived from the specific Comptonisation model (e.g. see Pietrini & Krolik 1995 and Beloborodov 2001). Since the model is linearised anyway, the precise form of the relation between photon index and cooling/heating ratio does not matter as much as the direction of the relation (which sets the sign of the lags). A positive correlation between Γ and the seed-to-heating luminosity ratio, arises naturally from conservation of both total luminosity and photon number in the corona. The assumption of thermal equilibrium is valid when the heating and cooling time-scales within the corona are small compared to the time-scales of variability of seed and heating luminosities. This should be the case for relatively compact coronae considered here.

To calculate the variation of a quantity $f(t)$ in response to a perturbing signal $s(t)$, we require the impulse response function (henceforth 'impulse response') for that quantity $g(\tau)$ (where τ is the time delay), so that the perturbation in $f(t)$, $\delta f(t) = \int_{-\infty}^{\infty} s(t-\tau) * g(\tau) \mathrm{d}\tau$. We will now derive the impulse responses for power-law continuum slope and flux variations, in terms of the coronal seed and heating variations.

For our simplified analytical calculation, we make the approximation that the seed photons are monochromatic with energy E_s, so that the total photon number is $L_\mathrm{s}/E_\mathrm{s}$. Assuming that total photon numbers are conserved during the Comptonisation process and that the cut-off photon energy $E_{cut} \gg E_\mathrm{s}$, the photon flux density variation at an energy E, $N(E,t)$ is given by:

$$N(E,t) = \frac{L_\mathrm{s}(t)(\Gamma(t) - 1)}{E_\mathrm{s}^2} \left(\frac{E}{E_\mathrm{s}} \right)^{-\Gamma(t)} \quad . \qquad (2)$$

By linearising Equations 1 and 2, i.e. assuming small perturbations in the time-variable parameters we obtain the impulse responses for $\Gamma(t)$ and $N(E,t)$:

$$g_\Gamma(\tau) = \langle \Gamma \rangle \beta \left(\frac{g_\mathrm{s}(\tau)}{\langle L_\mathrm{s} \rangle} - \frac{g_\mathrm{h}(\tau)}{\langle L_\mathrm{h} \rangle} \right) \qquad (3)$$

$$g_\mathrm{pl}(E,\tau) = \langle N(E) \rangle \left([1 - u(E)] \frac{g_\mathrm{s}(\tau)}{\langle L_\mathrm{s} \rangle} + u(E) \frac{g_\mathrm{h}(\tau)}{\langle L_\mathrm{h} \rangle} \right) \qquad (4)$$

where $u(E) = \beta \langle \Gamma \rangle \left(\ln(E/E_\mathrm{s}) - \frac{1}{\langle \Gamma \rangle - 1} \right)$ and angle brackets denote the time-averaged quantities which are perturbed by changes in the seed and heating luminosities. Those changes are themselves quantified in terms of their own impulse responses, g_s and g_h, which will depend on the physical system producing the seed and heating luminosities and their variations. We will determine these functions for the case of propagating accretion fluctuations in the next Section.

3 IMPULSE RESPONSES FROM A VARIABLE ACCRETION FLOW

We assume that the driving signals are mass accretion rate fluctuations propagating through the disk. For simplicity we will assume simple non-diffusive propagation, so that the amplitudes and power-spectral shapes of mass-accretion fluctuations are preserved as they propagate inwards. This approximation can be applied to 'classical' accretion disks provided that the fluctuation time-scale is comparable to or greater than the viscous time-scale at the radius it is generated (Churazov et al. 2001).

The response delay τ depends on the radial drift velocity of the accretion variations. Since the final model will combine signals from multiple radii, it is useful to define a fixed zero-delay at the innermost radius of the accretion flow, r_in, which allows us to define a fixed, negative, propagation time-delay for each radius r (in units of the gravitational radius R_g):

$$\tau(r) = \int_{r_\mathrm{in}}^{r} \mathrm{d}\tau = \int_{r_\mathrm{in}}^{r} \mathrm{d}r / v_r \qquad (5)$$

where v_r is the radial drift velocity $v_r = -\alpha(h/r)^2 r^{-1/2}$, for a disk with scale-height h and dimensionless viscosity parameter α. Note that the radial drift velocity is expressed as a fraction of c, so the delays are naturally expressed in units

of the light-crossing time for 1 R_g. For simplicity we assume that light-travel time lags, e.g from the disk to the corona, are negligible compared to the lags due to propagating fluctuations which we consider here. We have also assumed that $r_{\rm in}$ is the inner zero-torque boundary of the whole accretion flow (including the coronal part), which we assume to correspond to the innermost stable circular orbit (ISCO).

We define all luminosities as fractions of the total dissipated power from the flow. The power dissipated by the accretion flow in an annulus dr at radius r is therefore defined, using the usual radial dependence (e.g. Frank et al. 2002), as:

$$f_{\rm diss}(r)dr = \frac{r^{-2}[1 - (r_*/r)^{1/2}]dr}{\int_{r_{\rm in}}^{r_{\rm out}} r^{-2}[1 - (r_{\rm in}/r)^{1/2}]dr} \quad (6)$$

where $r_{\rm out}$ is the outer radius of the flow. At this stage we speak in terms of the accretion flow rather than the accretion disk, because we assume that the central compact corona is itself powered by accretion and may be thought of as a hot inner flow with radius $r_{\rm cor}$ which corresponds to the truncation radius of the blackbody-emitting disk. If we assume that all power dissipated within $r_{\rm cor}$ goes into heating the corona, we can define the coronal heating impulse response function $g_{\rm h}(\tau)$ as:

$$g_{\rm h}(\tau)d\tau = \begin{cases} f_{\rm diss}(r)dr, & \text{if } r_{\rm in} < r \leqslant r_{\rm cor} \\ 0, & \text{otherwise} \end{cases} \quad (7)$$

The impulse response function $g_{\rm d}(\tau)$ for direct disk blackbody emission due to dissipation is:

$$g_{\rm d,diss}(\tau)d\tau = \begin{cases} f_{\rm diss}(r)dr, & \text{if } r_{\rm cor} < r \leqslant r_{\rm fluc} \\ 0, & \text{otherwise} \end{cases} \quad (8)$$

where $r_{\rm fluc}$ is the starting radius of the accretion fluctuation (which we assume to begin in the disk, i.e. outside the corona). Note that we include the additional subscript 'diss' to make a distinction between disk (and seed) emission which is produced directly by dissipation in the flow, and that produced by heating of the disk by the coronal power-law emission.

Assuming that all photons reaching the corona become seed photons and that the fraction of disk photons reaching the corona from a radius r is $f_{\rm d\rightarrow c}(r)$, the seed photon impulse response due to disk photons produced by viscous dissipation is:

$$g_{\rm s,diss}(\tau)d\tau = \begin{cases} f_{\rm d\rightarrow c}(r)f_{\rm diss}(r)dr, & \text{if } r_{\rm cor} < r \leqslant r_{\rm fluc} \\ 0, & \text{otherwise} \end{cases} \quad (9)$$

The calculation of $f_{\rm d\rightarrow c}(r)$ depends on the assumed coronal geometry and is discussed in Appendix A. For the present work, we assume that the disk is the only source of seed photons for the corona. It would however, be possible to allow some fraction of the viscous dissipation powering the corona to be converted into internal seed photons, e.g. via synchrotron emission if the corona is magnetised (Veledina et al. 2013).

A fraction of the emitted total coronal luminosity (which is the sum of seed and heating luminosities) will be intercepted and reprocessed by the disk. For sufficiently high densities and/or low ionisation states, a significant component will be emitted with a thermal spectrum, producing a thermal X-ray reverberation signal which has a short, light-travel time

delay with respect to the illuminating coronal X-ray variations. This signal will track the total coronal luminosity variation with negligible delay in our propagating fluctuations model. Therefore our assumed reverberation component for the direct disk emission impulse response is given by:

$$g_{\rm d,rev}(\tau)d\tau = [g_{\rm s,diss}(\tau) + g_{\rm h}(\tau)]\,d\tau \cdot f_{\rm abs}\int_{r_{\rm cor}}^{r_{\rm out}} f_{\rm c\rightarrow d}(r)dr \quad (10)$$

Where $f_{\rm c\rightarrow d}(r)$ is the fraction *per unit radius* of coronal photons intercepted by the disk, as a function of radius (see Appendix A for details of its calculation) and $f_{\rm abs}$ is the fraction of the incident flux which is absorbed and reprocessed into disk blackbody emission. We assume $f_{\rm abs}$ to be constant with radius, although in principle it can be affected by radial changes in disk ionisation and/or density.

Some component of the direct disk photons produced by reverberation will re-enter the corona to act as an extra source of seed photons. To avoid double-counting of the same luminosity component, we assume that the reverberation luminosity returning to the corona does not itself contribute to further reprocessing in the disk. The reverberation component of the seed photon impulse response is thus given by:

$$g_{\rm s,rev}(\tau)d\tau = [g_{\rm s,diss}(\tau) + g_{\rm h}(\tau)]\,d\tau \\ \cdot f_{\rm abs}\int_{r_{\rm cor}}^{r_{\rm out}} f_{\rm d\rightarrow c}(r)f_{\rm c\rightarrow d}(r)dr \quad (11)$$

The final total direct disk and seed photon impulse responses are:

$$g_{\rm d}(\tau)d\tau = [g_{\rm d,diss}(\tau) + g_{\rm d,rev}(\tau)]d\tau \quad (12)$$

$$g_{\rm s}(\tau)d\tau = [g_{\rm s,diss}(\tau) + g_{\rm s,rev}(\tau)]d\tau \quad (13)$$

The time-averaged luminosities for the heating, direct disk and seed components can be determined by integrating the impulse responses over all radii (i.e. over all delays).

The impulse responses derived above can be used to determine spectral-timing properties in response to a mass-accretion fluctuation signal which originates at a single radius $r_{\rm signal}$. In reality it is likely that propagating fluctuations originate over a range of radii, as surmised by the propagating fluctuations model of Lyubarskii (1997) and supported by the broadband nature of the observed power spectra and multi-time-scale rms-flux relations observations (e.g. see discussion in Uttley et al. 2005) as well as MHD simulations of accretion flows (Hogg & Reynolds 2016). Since the simple impulse response functions described above map delay times on to unique radii, it is simple to model multi-location signals by using the same impulse responses but with different starting delays. Given a starting radius $r_{\rm signal}$ we can use Equation 5 to define a starting delay time $\tau_{\rm signal}$, which is negative since we define the innermost delay to be zero. The impulse response $g_{\rm signal}$ 'seen' by that fluctuating signal is then related to the overall impulse response $(g(\tau, E))$ calculated for that component by:

$$g_{\rm signal}(\tau) = \begin{cases} g(\tau) & \text{if } \tau \geqslant \tau_{\rm signal} \\ 0, & \text{otherwise} \end{cases} \quad (14)$$

If we then define $n_{\rm signal}$ signals with Fourier power-spectra $P_{{\rm signal},i}(\nu)$ (where ν is the Fourier frequency), originating at

radii $r_{\text{signal},i}$ with corresponding time delays $\tau_{\text{signal},i}$, the resulting power-spectrum is given by:

$$P(\nu) = \sum_{i=1}^{n_{\text{signal}}} P_{\text{signal},i}(\nu)|G_{\text{signal},i}(\nu)|^2 \quad (15)$$

where $G_{\text{signal},i}(\nu)$ is the Fourier transform of the impulse response for $\tau_{\text{signal},i}$ given by Equation 14. The cross-spectrum between two components, labelled 1 and 2 (e.g. two energies in the power-law, or the disk vs. a single power-law energy) is:

$$C_{1,2}(\nu) = \sum_{i=1}^{n_{\text{signal}}} P_{\text{signal},i}(\nu)G_{\text{signal},i,1}(\nu)G_{\text{signal},i,2}^*(\nu) \quad (16)$$

with frequency-dependent time-lag given by the argument of the cross-spectrum normalised by $2\pi\nu$.

For simplicity we assume that the power spectra of the individual mass-accretion rate fluctuation signals $P_{\text{signal},i}(\nu)$, are described by Lorentzian functions parameterised by a peak frequency $\nu_{\text{pk},i}$, quality-factor Q_i (approximately the frequency of the Lorentzian divided by its full-width at half maximum) and fractional rms rms_i. As discussed by Pottschmidt et al. (2003), the more common form of the Lorentzian function can then be calculated from these parameters, by calculating the resonance frequency $\nu_{\text{res},i} = \nu_{\text{pk},i}/\sqrt{1 + 1/(4Q_i^2)}$ and normalising factor $R_i = rms_i/\sqrt{0.5 - \tan^{-1}(-2Q_i)/\pi}$:

$$P_{\text{signal},i}(\nu) = \frac{2R_i^2 Q_i \nu_{\text{res},i}}{\pi \left(\nu_{\text{res},i}^2 + 4Q_i^2(\nu - \nu_{\text{res},i})^2\right)} \quad (17)$$

The number and radial location of Lorentzian signals and their parameters can be selected when setting up the model calculation and in principle can be arbitrary. However, the linear model described here does not account for viscous diffusion effects on mass accretion fluctuations as they propagate through the flow, which significantly suppresses variations on time-scales exceeding the local viscous propagation time-scale (e.g. see discussion in Churazov et al. 2001 and a more extensive treatment in Mushtukov et al. 2018). Therefore for simplicity, we will require that signal peak frequencies only correspond to time-scales which exceed the propagation delay through the flow from that radius.

The above equations and assumed input signal power spectra allow us to calculate the observed power spectra and lags expected from our model. It is important to note that this approach to combining signals from different radii assumes that the mass accretion rate variations combine additively instead of multiplicatively, as is implicit in the propagating fluctuations model (Uttley et al. 2005). We will consider the effects of this simplification in Appendix C, by comparing with lag predictions from numerical simulations of the propagating fluctuations.

4 RESULTS FOR DIFFERENT CORONAL GEOMETRIES

To calculate the disk, seed and heating impulse responses, we define 200 contiguous, geometrically spaced radial bins of radius r_j between $r_{\text{in}} = 2\,R_g$ (corresponding to dimensionless spin parameter $a = 0.94$) and $r_{\text{out}} = 300\,R_g$ (large enough to encompass almost the entire seed photon flux). To assign the time-delays of the impulse responses we assume that the delay due to propagation across the radial bin in units of R_g/c is $d\tau_j = k\sqrt{r_j}dr_j$ where k is a constant. For a standard disk, this prescription effectively assumes that the combination of disk parameters $k \simeq \alpha^{-1}(r/h)^2$ is constant with radius. In order to reproduce lags of similar amplitude to those observed we set $k = 100$ in the disk, corresponding to relatively fast variations from a slim or moderately thin disk with large α. We also start by assuming that $k = 10$ in the geometrically-thicker coronal part of the accretion flow.

To focus on the effects of accretion disk variability on the spectral-timing properties, we assume that mass accretion variations are generated continuously across the disk only, with no additional variability introduced within the corona. Input signals are generated at each radial bin for only the disk part of the accretion flow. In Appendix B we show that introducing intrinsic coronal accretion variability will likely only affect the spectral-timing properties at the highest Fourier frequencies, beyond what we consider here.

The Lorentzian disk variability signals have peak frequencies equal to the inverse of the radial delay time-scale $\nu_{\text{pk},j} = k^{-1}r_j^{-3/2}$, constant $Q_j = 1$ and constant $rms_j = 0.01/\sqrt{200}$. The choice of a constant signal rms across geometrically-spaced radial bins leads naturally to a power-spectral shape $P(\nu) \propto 1/\nu$ over a broad frequency range, similar to that observed in both soft and hard spectral states of BHXRBs (e.g. Heil et al. 2015). Our chosen rms value corresponds to an integrated accretion fluctuation rms of only 1%, but in our linear model, the value chosen is arbitrary as it simply scales all observed power-spectral amplitudes by the same factor, but does not affect their shapes. The magnitude of rms is important for considering non-linear effects, both due to power-law photon index variations and the multiplicative nature of mass accretion variations implied by the rms-flux relation. However, we use numerical simulations to show in Appendix C that these effects remain negligible for accretion fluctuations with integrated rms of 40%, consistent with the X-ray variability observed in hard state BHXRBs.

4.1 Impulse responses

The lags in coronal power-law emission are strongly dependent on the seed photon impulse response, which in turn depends on the coronal geometry. Here we consider two types of geometry: spherical (with radius r_{cor}) and an inverted cone geometry. The inverted cone shape (strictly speaking the frustum of an inverted cone, i.e. with the pointed end cut-off) is intended to represent a jet or wind-like corona or a cylindrically-shaped 'hot flow'. It has a basal coronal radius in the disk plane r_{cor} and coronal height above the disk plane h_{cor}. The radius at the top (widest) end of the cone is determine by the opening angle θ_{cor} which is the angle relative to the normal to the disk plane, such that $\theta_{\text{cor}} = 0°$ gives a cylindrical corona.

We consider the effects of changing the coronal radius (for both the spherical and inverted-cone geometries), and the coronal height and opening angle (for the inverted-cone geometry). Figure 1 shows the disk (solid lines), seed (dotted lines) and heating (dashed lines) impulse responses for these situations, with both the dissipated and reverberation contributions to the disk and seed components summed to give

those impulse responses. The delays are plotted using symmetric logarithmic axes with delays $> -100\ R_g/c$ plotted on a linear scale. The response units are luminosity per unit time delay, where luminosities are expressed as a fraction of the total dissipated accretion luminosity. The impulse responses are further multiplied by the absolute time delay, so that the delays which contribute the most to the impulse response appear as a peak.

The top panels in Fig. 1 show the case for changing coronal radius (where for the inverted cone geometry we fix $h_{\mathrm{cor}} = 10\ R_g$ and $\theta_{\mathrm{cor}} = 30°$). They are qualitatively similar for the spherical and inverted cone geometries, with accretion power being redistributed from disk emission to coronal heating as the coronal radius increases. However, the seed components and reverberation contributions are somewhat weaker for the spherical geometry due to the smaller solid angle presented by the spherical corona to the disk at larger heights.

The lower panels in Fig. 1 show the case for changing coronal height (with fixed $r_{\mathrm{cor}} = 10\ R_g$ and $\theta_{\mathrm{cor}} = 30°$) and changing coronal opening angle (with fixed $r_{\mathrm{cor}} = 10\ R_g$ and $h_{\mathrm{cor}} = 10\ R_g$). Since the coronal radius is the same in all cases, we also show the radii associated with signals produced with a given delay, which are indicated with vertical dashed lines. Although the disk and heating impulse responses are similar (as expected for fixed coronal radius), the seed impulse responses are strongly dependent on coronal height and opening angle. Moreover, the seed impulse responses show distinct evolution for each parameter.

Changes in coronal height lead to stronger changes in the peak delay of the seed impulse response compared to changes in opening angle, while opening angle affects the luminosity of seed photons more than the coronal height. These differences arise due to the different dependencies of $f_{\mathrm{d}\to\mathrm{c}}(r)$ on the coronal geometry parameters (see Fig. A1). An increase in coronal height causes the corona to respond more to seed variations from larger radii, with the largest effects for disk radii exceeding the radius at the top of the corona r_{top}, which contribute large delays albeit with relatively weaker disk emission. Conversely, increases in coronal opening angle increase the disk luminosity intercepted by the corona across all radii by broadly similar amounts, with the largest differences at intermediate radii $\sim r_{\mathrm{top}}$.

4.2 Lags and power spectra

To calculate the expected time lags and power-spectra from the impulse responses shown in the previous section, we first calculate the power-law flux impulse response for soft, medium and hard energies $E_{\mathrm{soft}} = 3E_s$, $E_{\mathrm{med}} = 9E_s$ and $E_{\mathrm{hard}} = 27E_s$. The power-law lags are themselves independent of the choice of seed energy E_s. However, for a seed energy corresponding to the peak of a disk blackbody with maximum temperature kT_{max}, $E_s = 2.82kT_{\mathrm{max}}$ so that the relevant energies for a hard state disk with $kT_{\mathrm{max}} = 0.2$ keV are $E_s \simeq 0.56$ keV, $E_{\mathrm{soft}} \simeq 1.7$ keV, $E_{\mathrm{med}} \simeq 5.1$ keV and $E_{\mathrm{hard}} \simeq 15.2$ keV.

We rebin the geometrically spaced impulse response bins (which are given in units of R_g/c) to a uniform grid of time bins in units of seconds, with width dt_{bin} equal to the one quarter of the shortest propagation delay across a radial bin: $dt_{\mathrm{bin}} = \frac{1}{4}\frac{GM_{\mathrm{BH}}}{c^3}d\tau_{j,\mathrm{min}}$. To speed up our calculations, we choose $d\tau_{j,\mathrm{min}}$ to be the delay across the innermost disk ra-

dial bin at r_{cor} and sum the coronal impulse responses into a single adjacent delay bin of width dt_{bin}, i.e. we effectively treat the coronal delays as approaching zero. We show in Appendix B that this approximation only has a small effect on the calculated spectral-timing properties.

The rebinned impulse responses are padded with zeros so that they contain 262144 bins. We assume a black hole mass $M_{\mathrm{BH}} = 10\ M_\odot$, so for $r_{\mathrm{cor}} = 10\ R_g$ our final zero-padded impulse responses have $dt_{\mathrm{bin}} = 1$ ms and are ~ 262 s long. By keeping track of the corresponding start and stop impulse response bins for each of the geometrically spaced radial bins which contributes to the variability signal, we use Equations 14–16 to calculate the frequency-dependent spectral-timing properties.

Fig. 2 shows the resulting time lags and power spectra for disk and power-law emission, for the different coronal geometries with impulse responses shown in the corresponding panels in Fig. 1. To compare the power spectra (lower panels of each plot), we normalise them by the summed mass accretion rate signal power spectrum, $P \sum \dot{m}(r)$. By plotting this way, the energy-dependent filtering effect on the power spectrum remains clear. For further clarity we only show power spectra for the disk and medium and hard power-law bands since these latter bands can be observed free of disk emission in BHXRBs. We note for completeness that the soft power-law power spectrum continues the trend of greater high-frequency filtering at softer energies.

4.2.1 Low-frequency hard lags

At lower frequencies, the lags between power-law energies are constant with frequency. This reflects the fact that the seed photon response 'seen' by signals from larger radii does not evolve with radius, since all the response is contained within smaller radii (e.g. $< 20\ R_g$ in the lower panels of Fig. 1). The frequency where these power-law lags roll over towards smaller values should correspond to the frequencies of radii where the seed impulse response peaks, hence the stronger evolution of the lag roll-over frequency with r_{cor} or h_{cor}, compared to the evolution with θ_{cor}.

The power-law lag amplitude at low-frequencies corresponds to the difference in centroid delay values of the power-law flux impulse responses:

$$\langle\tau(E_2)\rangle - \langle\tau(E_1)\rangle \simeq \beta\langle\Gamma\rangle\left(\langle\tau_{\mathrm{h}}\rangle - \langle\tau_{\mathrm{s}}\rangle\right)\ln(E_2/E_1)\,, \quad (18)$$

where angle brackets denote centroid (mean) impulse response delay (photon index) values and we note that since the seed centroid $\langle\tau_{\mathrm{s}}\rangle$ is more negative than the coronal heating centroid $\langle\tau_{\mathrm{h}}\rangle$, the resulting lags are positive (hard) lags. We can immediately see that the low-frequency power-law lags scale log-linearly with the energy, as is commonly observed in the data (hence the lag amplitudes are identical for the equal differences in log-energy which are shown in the Figure). The log-linear behaviour is a natural result of spectral pivoting of a power-law with a delay between the power-law normalisation change and the power-law index change (e.g. see Kotov et al. 2001; Körding & Falcke 2004).

4.2.2 High-frequency soft lags

The lag of the soft power-law emission relative to the disk blackbody shows the most interesting behaviour. At low fre-
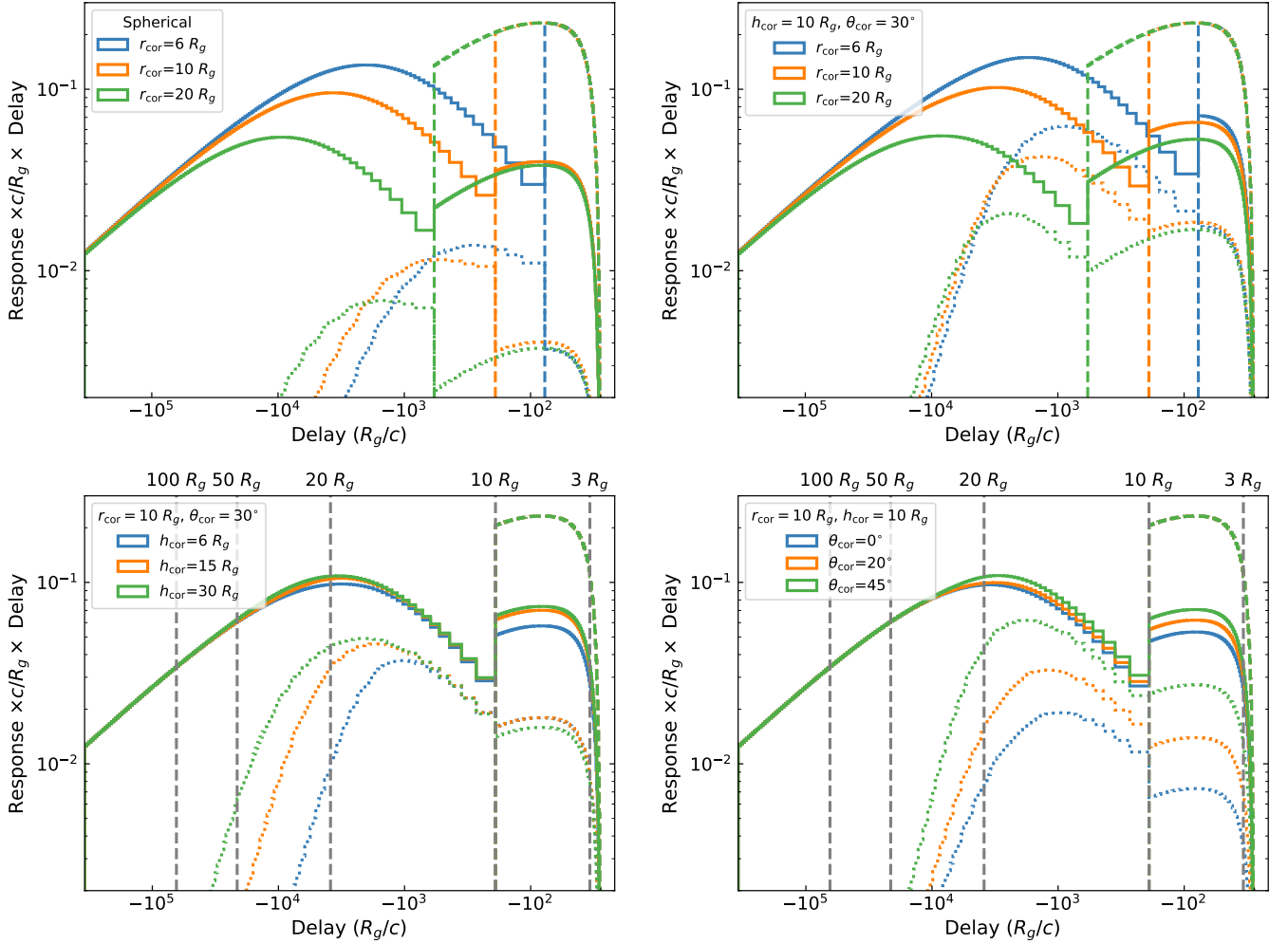
Figure 1. Comparison of impulse responses for different coronal geometries and parameter variations. *Top-left*: changing coronal radius r_{cor} for a spherical corona. Then clockwise from *top-right*: inverted cone corona with changing coronal radius r_{cor}; changing opening angle θ_{cor}; changing coronal height h_{cor}. For each changing parameter value the plots show the total disk (solid lines), seed (dotted lines) and heating (dashed lines) impulse responses. The lower panels with constant r_{cor} also show the radii associated with a given delay for that r_{cor}.

quencies the lags continue to increase down to the frequency of the lowest generated signal in the disk. This strongly frequency-dependent lag corresponds to the broad extent of the disk impulse response towards long delays since disk emission originates from all variable radii. The centroid delay of the disk impulse response therefore continues to increase in amplitude towards larger radii (and hence lower signal frequencies). As frequency increases, the disk lags start to roll over rapidly, at frequencies corresponding approximately to the radii producing the peak in the disk impulse response. However the detailed high frequency behaviour is also driven by the soft power-law impulse response and hence, in turn, by the seed impulse response.

In particular, we see that the power-law to disk lags do not go to zero at high frequencies *but become negative*, i.e. they correspond to 'soft' lags. This behaviour is remarkably reminiscent of the soft lags observed at similar frequencies in observations of black hole X-ray binaries (e.g. Uttley et al. 2011; De Marco et al. 2015; Kara et al. 2019) and it seems

probable that those observed lags are caused by the same effect. I.e. these are not due to reverberation light-travel delays (since in our model these are set to zero), they are associated with the effect of seed photons on the power-law impulse response.

To better understand the origin of the negative lags in our model, Fig. 3 shows, for different inverted-cone geometric parameters, the difference in impulse response centroid values for the disk and soft power-law emission, plotted as a function of the driving signal frequency (ν_{signal}). The driving frequency for a given radius is the Lorentzian peak frequency ($\nu_{pk,i}$) assumed for accretion fluctuations generated at that radius, and loosely corresponds to the Fourier frequency in the calculated spectral-timing products (excluding the effects of combining the overlapping Lorentzian contributions from different radii). To show a broad range of frequencies clearly, the centroid difference is further multiplied by the driving frequency, i.e the y-axis value shows the lag as a fraction of variability time-scale, analogous to a phase lag. Positive
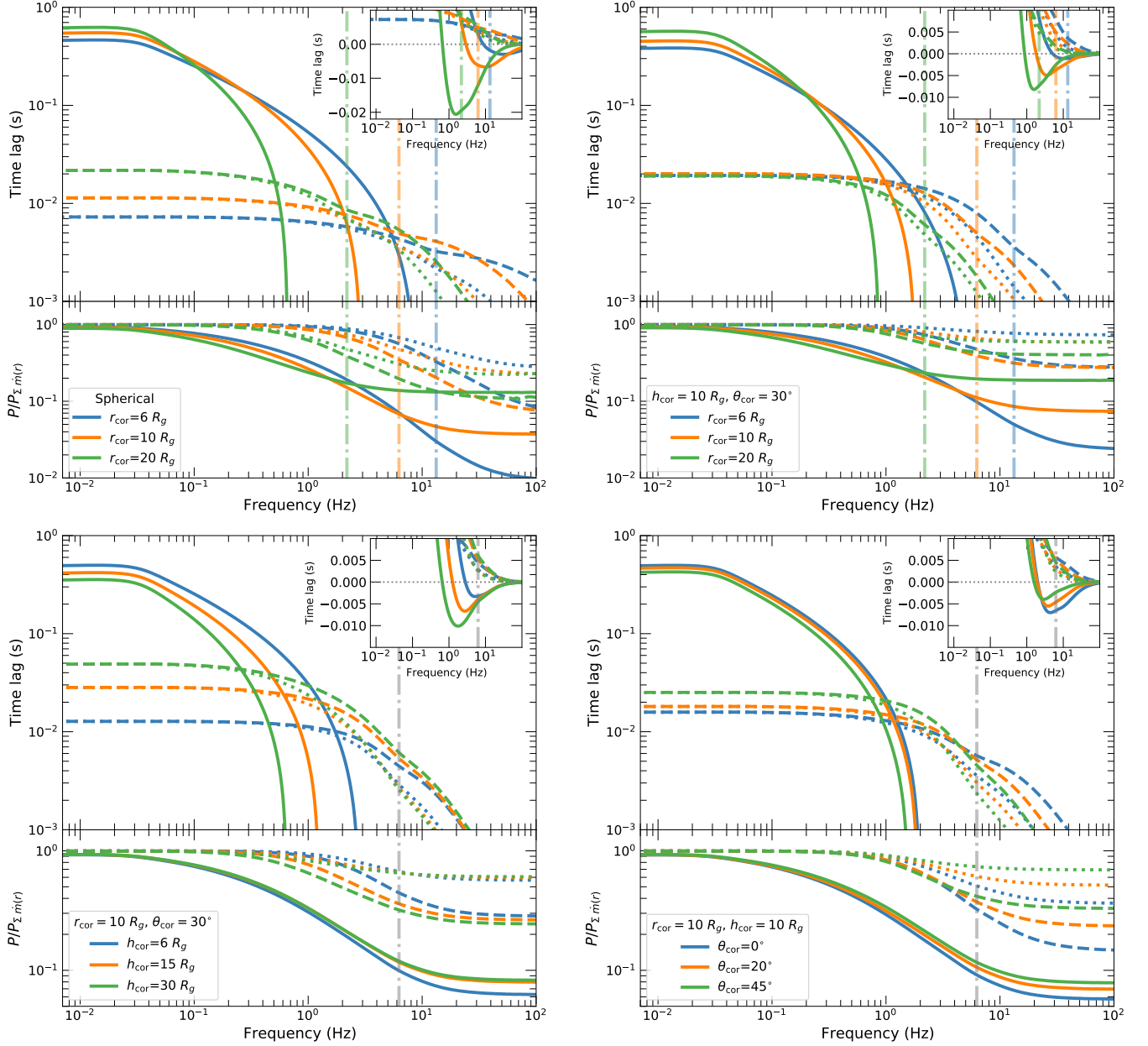
Figure 2. Comparison of spectral-timing properties, corresponding by position to the different coronal geometries with impulse responses shown in Fig. 1. For each plot, the *top panels* show time lags for power-law at E_{soft} vs. disk (solid line), power-law at E_{med} vs. E_{soft} (dashed), power-law at E_{hard} vs. E_{med} (dotted). Positive lags indicate that the harder band lags the softer band (or the power-law lags the disk). The *lower panels* show the ratio of emission power spectrum to integrated $\dot{m}$ power spectrum for disk (solid line) and power-law flux at E_{med} (dashed) and E_{hard} (dotted). The signal peak frequencies at r_{cor} are shown by the vertical dot-dashed lines.

differences in centroid value in the figure correspond to the soft power-law emission lagging the disk, but these switch to negative differences above frequencies which correspond roughly to the frequenies where the lags cross from positive to negative in the calculated lag-frequency spectra. There-fore, the negative lags result from the centroid differences and are not an artefact of the Fourier transform, e.g. due to phase-wrapping effects (Uttley et al. 2014).

To show the effects of the reverberation signal on the neg-ative lags, we also calculated the centroid differences in the absence of reverberation effects (dashed lines in Fig 3), by

setting the fraction of coronal luminosity that is absorbed and reprocessed by the disk to zero. Although it is not the only cause of the negative lags, reverberation does play a significant role in enhancing the amplitude of the negative lags and lowering the frequencies where they are seen. To un-derstand the effect of reverberation, first consider that the reverberation-only parts of the disk and seed impulse re-sponses (to the right of the vertical dashed lines correspond-ing to r_{cor} in Fig. 1) shift the total (propagation plus re-verberation) centroids for those components to smaller delay values. The relative shift is larger for signals from smaller
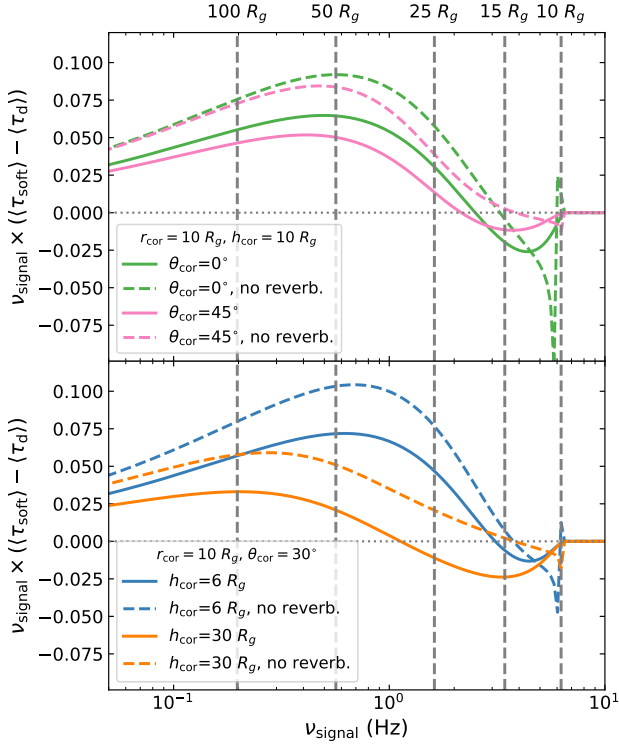
Figure 3. Difference between soft power-law and disk impulse response centroids as a function of driving signal frequency. Some corresponding signal radii are shown using vertical grey dashed lines. Different-coloured lines show different parameters of the inverted-cone coronal geometry (*upper panel*: different $\theta_{\rm cor}$, *lower panel*: different $h_{\rm cor}$). Centroid differences calculated with reverberation effects absent, are shown as dashed lines.

disk radii with correspondingly smaller delays due to propagation. Furthermore, this shift is greater for the disk than for the seed photons, since the seed photon reverberation-only component is relatively weak, because only a small fraction of photons from reverberation return again to the corona. Finally, since the soft power-law emission centroid is weighted towards the seed photon centroid (see Equation 4), we see that above a certain signal frequency, the disk centroid becomes smaller (less negative) than that of the soft power-law, leading to negative lags between disk and soft power-law.

Even in the absence of reverberation, the lags can still become negative at high frequencies. Using Equation 4 and approximating the coronal heating impulse response as a delta function at $\tau = 0$, the power-law flux centroid for a signal originating at a delay $\tau_{\rm signal}$ is:

$$\langle \tau_{\rm signal}(E) \rangle = \langle \tau_{\rm s,signal} \rangle \frac{1 - u(E)}{1 - u(E)(1 - f_s^{-1})} \qquad (19)$$

where $\langle \tau_{\rm s,signal} \rangle$ is the corresponding seed photon centroid value for the signal and $f_s = \int_{\tau_{\rm signal}}^{0} g_s(\tau){\rm d}\tau / \langle L_s \rangle$ is the fraction of total seed luminosity with delays $\tau > \tau_{\rm signal}$. Since $f_s \leqslant 1$, negative values of $u(E)$ lead to $|\langle \tau_{\rm signal}(E) \rangle| > |\langle \tau_{\rm s,signal} \rangle|$. This applies when $\langle \Gamma \rangle < 1 + 1/\ln(E/E_s)$. The effect arises due to pivoting of the power-law caused by seed photon variations while coronal heating remains constant. Total energy conservation means that flatter power-law spectra pivot at higher energies compare with steeper power-law

spectra. This leads to a stronger variation at low energies, which causes the delay to be enhanced.

4.3 Dependence of observable spectral-timing properties on coronal geometry

5 DISCUSSION

6 CONCLUSIONS

ACKNOWLEDGMENTS

REFERENCES

Arévalo P., Uttley P., 2006, MNRAS , 367, 801
Arévalo P., Papadakis I. E., Uttley P., McHardy I. M., Brinkmann W., 2006, MNRAS , 372, 401
Beloborodov A. M., 2001, Advances in Space Research, 28, 411
Böttcher M., 2001, ApJ, 553, 960
Chartas G., Kochanek C. S., Dai X., Poindexter S., Garmire G., 2009, ApJ, 693, 174
Churazov E., Gilfanov M., Revnivtsev M., 2001, MNRAS , 321, 759
De Marco B., Ponti G., Cappi M., Dadina M., Uttley P., Cackett E. M., Fabian A. C., Miniutti G., 2013, MNRAS , 431, 2441
De Marco B., Ponti G., Muñoz-Darias T., Nandra K., 2015, ApJ, 814, 50
Done C., Gierliński M., Kubota A., 2007, A&ARv, 15, 1
Fabian A. C., et al., 2009, Nature, 459, 540
Frank J., King A., Raine D. J., 2002, Accretion Power in Astrophysics: Third Edition. Cambridge Univ. Press, Cambridge
Giannios D., Kylafis N. D., Psaltis D., 2004, A&A , 425, 163
Heil L. M., Uttley P., Klein-Wolt M., 2015, MNRAS , 448, 3339
Hogg J. D., Reynolds C. S., 2016, ApJ, 826, 40
Kara E., et al., 2015, MNRAS , 446, 737
Kara E., et al., 2019, Nature, 565, 198
Kazanas D., Hua X.-M., Titarchuk L., 1997, ApJ, 480, 735
Körding E., Falcke H., 2004, A&A , 414, 795
Kotov O., Churazov E., Gilfanov M., 2001, MNRAS , 327, 799
Kroon J. J., Becker P. A., 2016, ApJ, 821, 77
Lyubarskii Y. E., 1997, MNRAS , 292, 679
MacLeod C. L., et al., 2015, ApJ, 806, 258
Makishima K., et al., 2008, PASJ, 60, 585
Miller J. M., et al., 2015, ApJ, 799, L6
Misra R., 2000, ApJ, 529, L95
Miyamoto S., Kitamoto S., Mitsuda K., Dotani T., 1988, Nature, 336, 450
Mushtukov A. A., Ingram A., van der Klis M., 2018, MNRAS , 474, 2259
Nowak M. A., Wilms J., Dove J. B., 1999, ApJ, 517, 355
Nowak M. A., et al., 2011, ApJ, 728, 13
Papadakis I. E., Nandra K., Kazanas D., 2001, ApJ, 554, L133
Pietrini P., Krolik J. H., 1995, ApJ, 447, 526
Pottschmidt K., et al., 2003, A&A , 407, 1039
Poutanen J., Fabian A. C., 1999, MNRAS , 306, L31
Rapisarda S., Ingram A., Kalamkar M., van der Klis M., 2016, MNRAS , 462, 4078
Reig P., Kylafis N. D., Giannios D., 2003, A&A , 403, L15
Shapiro S. L., Lightman A. P., Eardley D. M., 1976, ApJ, 204, 187
Timmer J., Koenig M., 1995, A&A , 300, 707
Uttley P., McHardy I. M., Vaughan S., 2005, MNRAS , 359, 345
Uttley P., Wilkinson T., Cassatella P., Wilms J., Pottschmidt K., Hanke M., Böck M., 2011, MNRAS , 414, L60
Uttley P., Cackett E. M., Fabian A. C., Kara E., Wilkins D. R., 2014, A&ARv, 22, 72
Veledina A., Poutanen J., Vurm I., 2013, MNRAS , 430, 3196
Wilkins D. R., Cackett E. M., Fabian A. C., Reynolds C. S., 2016, MNRAS , 458, 200

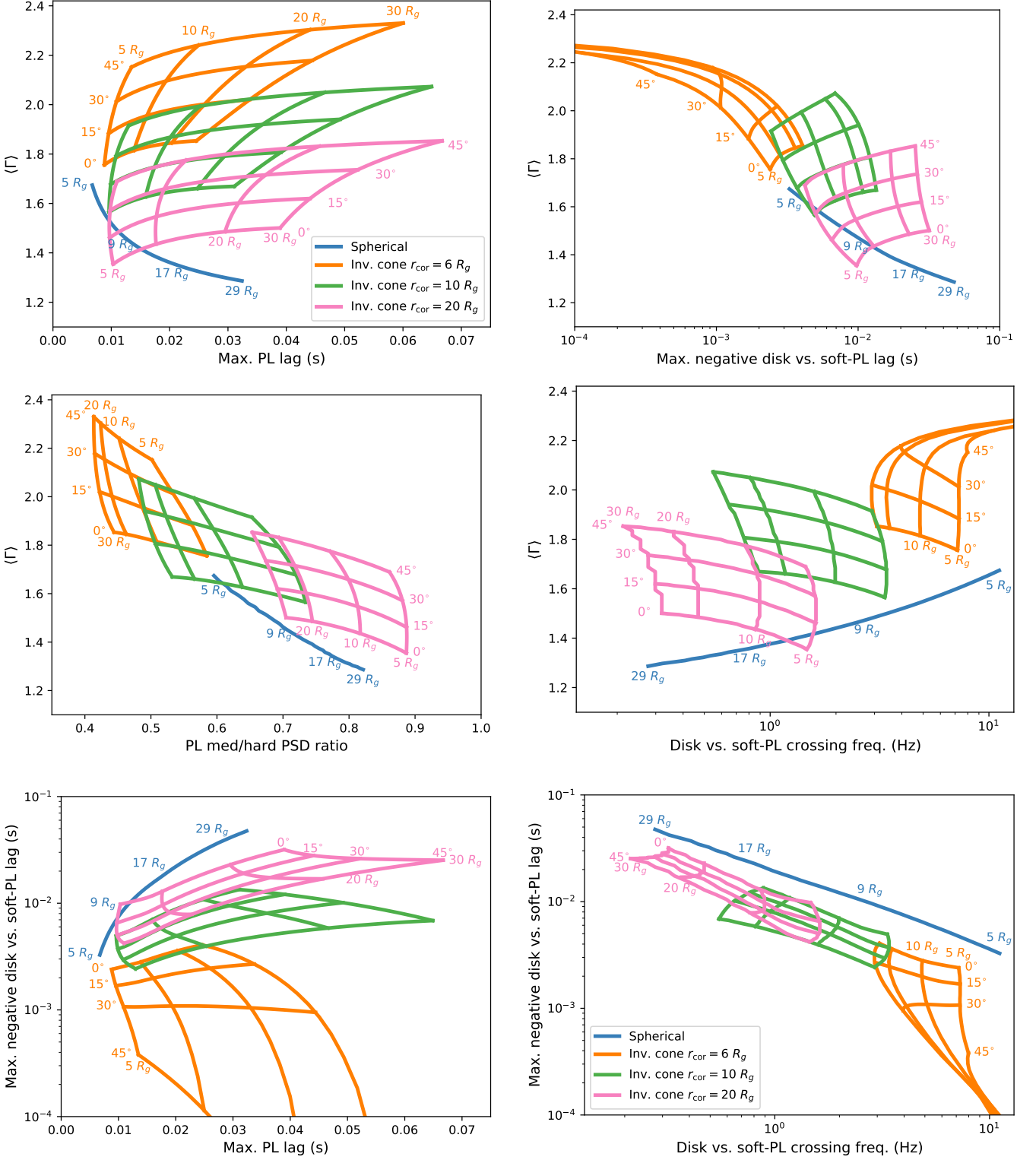**Figure 4.** Observables.

Zdziarski A. A., Poutanen J., Mikolajewska J., Gierlinski M., Ebisawa K., Johnson W. N., 1998, MNRAS , 301, 435

Zoghbi A., Fabian A. C., Reynolds C. S., Cackett E. M., 2012, MNRAS , 422, 129

Zoghbi A., et al., 2017, ApJ, 836, 2

This paper has been typeset from a TEX/LATEX file prepared by the author.

APPENDIX A: CORONAL GEOMETRY CALCULATIONS

For simplicity we calculate the fractions of photons intercepted by the corona from the disk, and vice versa, by assuming that the corona interacts with light as a solid body. Neglecting gravitational light-bending and Doppler beaming, the fraction of disk photons from a radius r that are intercepted by the corona, $f_{d\rightarrow c}(r)$, depends on the solid angle subtended by the corona as seen from r, as well as a weighting by the cosine of the angle between the direction to the corona and the normal to the disk plane (Lambert's cosine law):

$$f_{d\rightarrow c}(r) = \int_{\Omega_{cor}} \hat{\mathbf{n}}_d.d\mathbf{\Omega}_{cor} \Big/ \int_{2\pi} \hat{\mathbf{n}}_d.d\mathbf{\Omega}_{sph}$$
$$= \frac{1}{\pi} \int_{\Omega_{cor}} \hat{\mathbf{n}}_d.d\mathbf{\Omega}_{cor} \tag{A1}$$

Here Ω_{cor} and Ω_{sph} are the solid angles of the visible surface of the corona seen from the location on the disk at r and a sphere of visibility centred on the same location, $\hat{\mathbf{n}}_d$ is the unit vector normal to the disk plane and $d\mathbf{\Omega} = \hat{\mathbf{p}}\,d\Omega$ where $d\Omega$ is the solid angle of a surface element of the sphere of visibility or a *visible* (i.e. not self-obscured) surface element of the corona as seen from the disk location at r and $\hat{\mathbf{p}}$ is the unit vector pointing towards that disk location from the surface element. By assuming cylindrical symmetry, the calculated fraction applies to emission from the entire disk radius r and not just the single disk location calculated for.

Note that in general, the solid angle of a surface element with area dA as seen from the disk at radius r is given by $d\Omega = \hat{\mathbf{p}}.\hat{\mathbf{n}}_\epsilon\,dA/p^2$, where $\hat{\mathbf{n}}_\epsilon$ is the unit vector normal to the surface element and p is the magnitude of the position vector $\mathbf{p}$ from the disk location to the surface element, i.e. $\mathbf{p} = p\hat{\mathbf{p}}$. Surface elements with $d\Omega < 0$ are ignored, as these elements face away from the disk location calculated for and hence are obscured in the simple geometries assumed here.

For calculating $f_{c\rightarrow d}$, we assume that the corona has constant intrinsic surface brightness, with luminosity per unit surface area given by the total coronal luminosity divided by the total emitting surface area of the corona A_{cor}. With this simplifying assumption the fraction per unit radius of coronal photons intercepted by the disk is given by:

$$f_{c\rightarrow d}(r) = \frac{2\pi r f_{d\rightarrow c}(r)}{A_{cor}} \tag{A2}$$

For a spherical corona of radius r_{cor}, we can solve Eqn. A1 analytically to obtain:

$$f_{d\rightarrow c}(r) = \frac{1}{\pi}\left[\arcsin\left(\frac{r_{cor}}{r}\right) - \sqrt{\left(\frac{r_{cor}}{r}\right)^2 - \left(\frac{r_{cor}}{r}\right)^4}\right] \tag{A3}$$

with $f_{c\rightarrow d}(r)$ obtained from Eqn. A2 assuming $A_{cor} = 2\pi r_{cor}^2$ (since we only consider the coronal hemisphere on the observable side of the disk).

For the inverted cone corona modelled in this work, we solve Eqn. A1 numerically by splitting the corona into surface elements defined by a grid of 1000×1000 bins in azimuth (from 0 to 2π) and coronal height (from 0 to h_{cor}). To calculate $f_{c\rightarrow d}(r)$ we use $A_{cor} = \pi\left(r_{top}^2 + (r_{cor} + r_{top})\sqrt{(r_{top} - r_{cor})^2 + h_{cor}^2}\right)$, where r_{top} is the radius of the top surface of the corona ($r_{top} = r_{cor} + h\tan\theta_{cor}$).

Figure A1 shows $f_{d\rightarrow c}(r)$ calculated for the different geometries and inverted corona parameters, to demonstrate the effects of changing coronal height and opening angle (see Section 4.1 for further discussion of these graphs).

APPENDIX B: PROPAGATION WITHIN THE CORONA

Since the accretion flow within r_{cor} is expected to be geometrically thick compared with the disk, mass accretion propagation speeds within the corona should be significantly faster than within the disk. To generate our initial impulse responses shown in Fig. 1 we assume propagation time-scale scaling factors of $k = 100$ and $k = 10$ times the dynamical time in the disk and corona respectively, although this difference may be conservative, since for geometrically thick coronae we could expect k to be as low as 1. To speed up our calculations in Section 4, we approximate the coronal propagation delay to be instantaneous with all coronal components of the impulse response (heating and associated reverberation and seed components) given a delay width equal to the time resolution of the simulation.

To show the effects of this simplifying assumption, we show in Figure B1 the frequency-dependent spectral-timing properties for the instantaneous coronal delay (coronal propagation velocity $v_{r,cor} = \infty$) and $k = 10$ coronal propagation time ($v_{r,cor} = 0.1r^{-1/2}$), for the inverted cone coronal geometry with $r_{cor} = 10\,R_g$, $h_{cor} = 10\,R_g$, $\theta_{cor} = 30°$. We also consider the situation ($rms_{i,cor} = rms_{i,disk}$) where variability is introduced into the corona as well as the disk, such that each geometrically spaced annulus in the corona (with $r < r_{cor}$) introduces a signal with Lorentzian frequency following the disk scaling of frequency with radius and q-value and rms amplitude the same as that produced in the disk annuli.

The spectral-timing properties show little difference at frequencies $\nu < \nu_{cor}$ as might be expected. Towards higher frequencies, the extended impulse response caused by finite coronal propagation speeds leads to a small enhancement of the time lags and suppression of high frequency power. Introducing variability signals within the corona leads to a more substantive change at high frequencies, since for $\nu > \nu_{cor}$ the luminosity in the coronal heating (and associated reverberation) impulse response decreases with signal frequency. This is because higher-frequency signals originate from smaller radii in the corona, and thus modulate a smaller fraction of the dissipated accretion power.

Overall, we conclude that the main observable spectral-timing properties that are introduced by the delay between disk seed photon and coronal heating variation, such as the maximum hard and soft lags and ν_{cross}, are not significantly altered by incorporating the speed of coronal propagation or intrinsic coronal variability. Spectral-timing behaviour at higher frequencies ($> \nu_{cor}$) may be affected however.

APPENDIX C: TEST OF LINEARITY WITH TIME-SERIES SIMULATIONS

We can test the validity of our use of linear impulse response functions to calculate the spectral-timing properties of our model using stochastic time-series simulations of a simplified variable accretion flow. Here we follow the approach of Arévalo & Uttley (2006) and use the method of Timmer & Koenig (1995) to simulate a time series of fractional accretion rate modulation, $\dot{m}_i(t)$ (normalised to a mean $\langle\dot{m}_i(t)\rangle = 1$) for each annulus of the disk corresponding to radius r_i, using the Lorentzian parameters associated with each radius to determine the $\dot{m}_i(t)$ power spectrum. The physical accretion rate time-series $\dot{M}_i(t)$ for a given radius is produced by multiplying together the $\dot{m}(t)$ generated at that radius with the physical time-series generated for the preceding (outer) radius and shifting the resulting signal by the propagation delay across the radial bin, $\Delta\tau_i$:

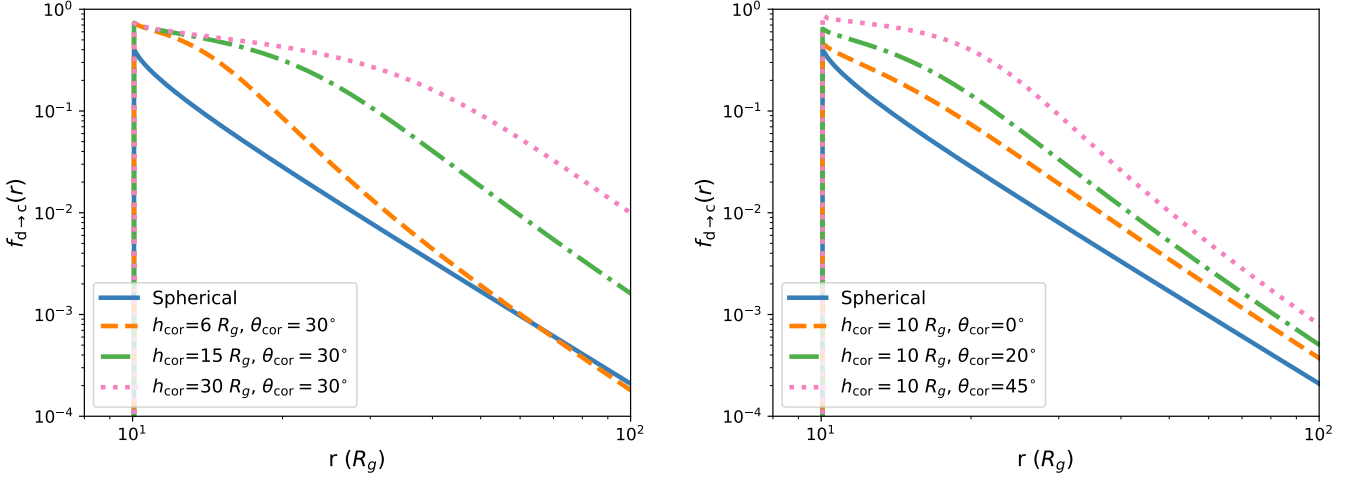$$\dot{M}_i(t + \Delta\tau_i) = \dot{m}_i(t)\dot{M}_{i+1}(t) \tag{C1}$$

Figure A1. Comparison of the radially-dependent fraction of disk photons intercepting the corona $f_{d \to c}(r)$, for a spherical corona and an inverted cone corona with varying scale-height (left panel) and opening angle (right panel). All cases shown have coronal radius $r_{cor} = 10 R_g$.
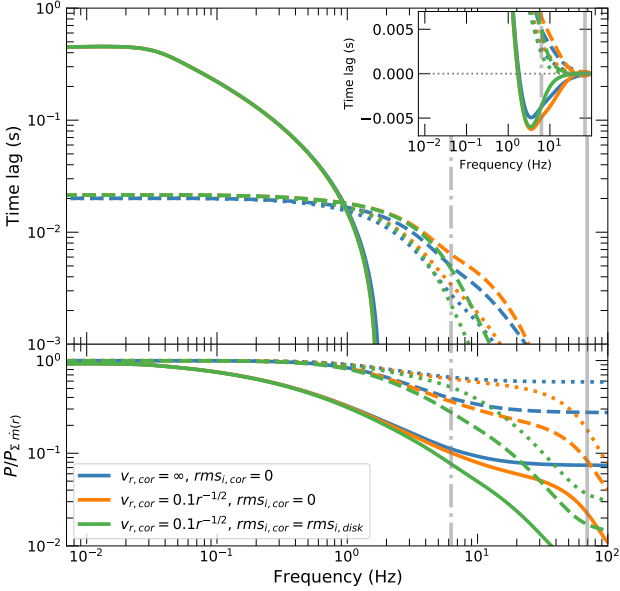

Figure B1. Frequency-dependent spectral-timing properties for different types of coronal propagation (instantaneous, fast propagation with no intrinsic coronal variability, fast propagation with intrinsic coronal variability), assuming $r_{cor} = 10 R_g$, $h_{cor} = 10 R_g$, $\theta_{cor} = 30°$ in all cases. *Top panel*: time lags for power-law at E_{soft} vs. disk (solid line), power-law at E_{med} vs. E_{soft} (dashed), power-law at E_{hard} vs. E_{med} (dotted). Positive lags indicate that the harder band lags the softer band (or the power-law lags the disk). *Lower panel*: ratio of emission power spectrum to integrated $\dot{m}$ power spectrum for disk (solid line) and power-law flux at E_{med} (dashed) and E_{hard} (dotted). The signal frequencies at r_{cor} and r_{in}, ν_{cor} and ν_{in} are shown by the vertical dot-dashed and solid grey lines respectively.

By repeating this calculation for successive inwards radii, we can generate an accretion fluctuation time series for each radius, from which we can determine the dissipation power time series for each radius, by multiplying by $f_{diss}(r_i$, calculated from Equation 6). This can in turn be used to generate the disk dissipation and coro-

nal heating time series associated with each radius, the seed contribution from disk dissipation (using $f_{d \to c}(r_i)$ and from summing their totals over all radii we can determine the total heating, disk and seed light curves, including reverberation contributions to the disk and seed contributions (by applying $f_{c \to d}(r_i)$. Finally, we can use the generated time-series directly in Equation 1 to determine a time-series for photon index Γ, and use Equation 2 to determine the power-law flux at a given energy.

This approach provides a numerical $non-linear$ time-series method for calculating spectral-timing properties using our lags model. The method is non-linear for two reasons. Firstly the generated accretion rate time-series are formally non-linear, incorporating the rms-flux relation and log-normal flux distributions that are observed in the X-ray variability of accreting black holes (Uttley et al. 2005). Secondly, the power-law flux variations are generated from the full, non-linear versions of Equations 1 and 2 rather than the linearised versions that are used to determine the impulse responses of the power-law flux.

Figure C1 shows the spectral-timing results of our numerical simulation assuming an inverted cone coronal geometry, with rms amplitude of accretion variability set to be 40 per cent, consistent with variations often observed in the hard state. For the simulation, 10 sets of time-series are generated, each consisting of 524288 bins with time resolution of 1 ms, for a simulation equivalent to 5243 s of data. The simulated light curves are split into segments of 65536 bins ($\sim$ 65.5 s) for calculation of the spectral timing products, which are further binned geometrically in frequency, with geometric binning factor 1.05. For comparison we show the corresponding results for the impulse response approach that is used in this work. The only significant deviations that can be seen at low frequencies are due to the intrinsic noise variability of the introduced time-series, which lead to fluctuations in the time-lags and the signal power (and hence the power spectra of emission). At higher frequencies this noise in the simulated data is smoothed over, but small shifts in the power spectra can be seen with power enhanced at high frequencies in the simulated data. No differences are seen in the lags however. The increase in the high-frequency power from the simulated data is a known effect of the multiplicative variability process used to generate the light curves (Uttley et al. 2005). However, like the lags, power-spectral ratios between different bands are not changed significantly. We conclude that even for relatively large amplitudes of variability, our linear impulse response model is an excellent approximation to the full non-linear model.
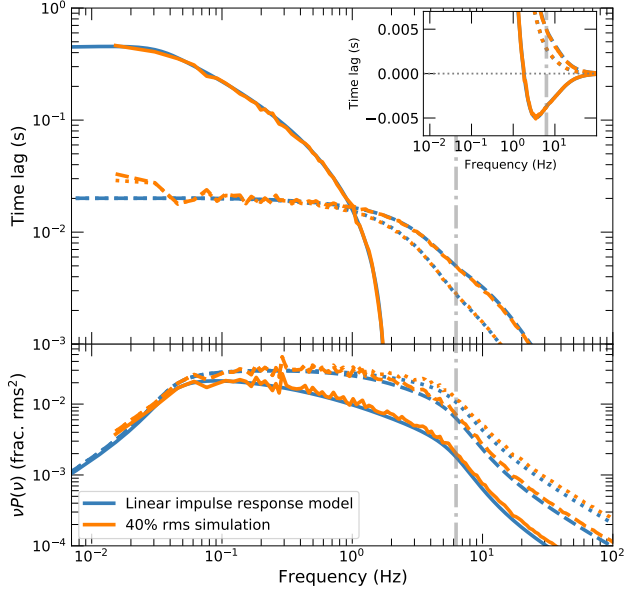
Figure C1. Comparison of frequency-dependent spectral-timing properties for numerical simulations of our lags model using a simplified accretion flow with 40 per cent rms variability of accretion rate, versus the results obtained from linear impulse response calculations, assuming an inverted cone corona with $r_{\rm cor} = 10 \ R_g$, $h_{\rm cor} = 10 \ R_g$, $\theta_{\rm cor} = 30°$. *Top panel*: time lags for power-law at $E_{\rm soft}$ vs. disk (solid line), power-law at $E_{\rm med}$ vs. $E_{\rm soft}$ (dashed), power-law at $E_{\rm hard}$ vs. $E_{\rm med}$ (dotted). Positive lags indicate that the harder band lags the softer band (or the power-law lags the disk). *Lower panel*: power spectra for disk (solid line) and power-law flux at $E_{\rm med}$ (dashed) and $E_{\rm hard}$ (dotted). The signal peak frequency at $r_{\rm cor}$ is shown by the vertical dot-dashed grey line.